LIMNOLOGY and OCEANOGRAPHY

ASLO

*Limnol. Oceanogr.* 9999, 2020, 1–16

doi: 10.1002/lno.11431

# The interaction of physical and biological factors drives phytoplankton spatial distribution in the northern California Current

**Jeffrey W. Krause**,[1,2*] **Mark A. Brzezinski**,[3,4] **John L. Largier**,[5,6] **Heather M. McNair**,[3,4,a] **Michael Maniscalco**,[3,4] **Kay D. Bidle**,[7] **Andrew E. Allen**,[8,9] **Kimberlee Thamatrakoln**[7]

[1]Dauphin Island Sea Lab, Dauphin Island, Alabama
[2]Department of Marine Sciences, University of South Alabama, Mobile, Alabama
[3]Marine Science Institute, University of California Santa Barbara, Santa Barbara, California
[4]Department of Ecology Evolution and Marine Biology, University of California Santa Barbara, Santa Barbara, California
[5]Coastal & Marine Sciences Institute, University of California Davis, Bodega Bay, California
[6]Department of Environmental Science & Policy, University of California Davis, Bodega Bay, California
[7]Department of Marine and Coastal Sciences, Rutgers University, New Brunswick, New Jersey
[8]Microbial and Environmental Genomics, J. Craig Venter Institute, La Jolla, California
[9]Scripps Institution of Oceanography, University of California San Diego, La Jolla, California

## *Abstract*

Transitions in phytoplankton community composition are typically attributed to ecological succession even in physically dynamic upwelling systems like the California Current Ecosystem (CCE). An expected succession from a high-chlorophyll (~ 10 $\mu g\ L^{-1}$) diatom-dominated assemblage to a low-chlorophyll (< 1.0 $\mu g\ L^{-1}$) non-diatom dominated assemblage was observed during a 2013 summer upwelling event in the CCE. Using an interdisciplinary field-based space-for-time approach leveraging both biogeochemical rate measurements and metatranscriptomics, we suggest that this successional pattern was driven primarily by physical processes. An annually recurring mesoscale eddy-like feature transported significant quantities of high-phytoplankton-biomass coastal water offshore. Chlorophyll was diluted during transport, but diatom contributions to phytoplankton biomass and activity (49–62% observed) did not decline to the extent predicted by dilution (18–24% predicted). Under the space-for-time assumption, these trends infer diatom biomass and activity and were stimulated during transport. This is hypothesized to result from decreased contact rates with mortality agents (e.g., viruses) and release from nutrient limitation (confirmed by rate data nearshore), as predicted by the Disturbance-Recovery hypothesis of phytoplankton bloom formation. Thus, the end point taxonomic composition and activity of the phytoplankton assemblage being transported by the eddy-like feature were driven by physical processes (mixing) affecting physiological (release from nutrient limitation, increased growth) and ecological (reduced mortality) factors that favored the persistence of the nearshore diatoms during transit. The observed connection between high-diatom-biomass coastal waters and non-diatom-dominated offshore waters supports the proposed mechanisms for this recurring eddy-like feature moving seed populations of coastal phytoplankton offshore and thereby sustaining their activity.

Spatial and temporal heterogeneity in phytoplankton abundance is typically explained using ecological theory where the phytoplankton group with physiological traits best matched to environmental conditions becomes the most abundant (Tilman 1977; Tilman et al. 1982). Trait-based approaches have been used to explain broad patterns in phytoplankton distribution or temporal succession observed in the field (Margalef 1978; Reynolds 1984). The interaction between physical and biological/ecological factors in determining phytoplankton succession is beginning to be understood. For instance, mesoscale physical processes can sustain high phytoplankton biomass over time, (e.g., Gaube et al. 2013), and play a dominant role in determining phytoplankton spatial distribution on timescales similar to or faster than those of ecological interactions (d'Ovidio et al. 2010).

The California Current Ecosystem (CCE) during the upwelling season is an ideal setting to better understand the interactions

*Correspondence: jkrause@disl.edu

Additional Supporting Information may be found in the online version of this article.

[a]Current Address: Graduate School of Oceanography, University of Rhode Island

between physical and biological/ecological factors in determining phytoplankton succession. Nearshore studies during upwelling favorable conditions frequently see rapid phytoplankton community evolution from dominance by diatoms toward dinoflagellate dominance that is concurrent with declines in macronutrient concentrations (Lassiter et al. 2006; Wilkerson et al. 2006). Regional numerical modeling has shown that mesoscale eddies are important for the transport of high-biomass and high-nutrient coastal waters offshore (Nagai et al. 2015) and direct observation at offshore mesoscale fronts has shown these sites to be major zones of organic matter export due to both gravitational sinking and subduction (Stukel et al. 2017). While the transport of high-biomass phytoplankton seed populations from coastal to offshore waters has also been inferred from observations of surface currents (Halle and Largier 2011), we know of no direct observations that combine phytoplankton standing stocks, physiological rate processes and transcriptomics to understand the transport of high-biomass, upwelling-driven phytoplankton assemblages offshore in the CCE.

Ship-board observations to ground truth remote-sensing data are lacking, especially those associated with biological data. To overcome this issue, Cianelli et al. (2017) merged data from a fixed time-series site with spatially resolved current data to suggest that physical and biological factors affect phytoplankton distribution individually or in concert. Villar et al. (2015) integrated field surveys with modeling efforts to provide a more synoptic view of how phytoplankton cycle nutrients in eddies during transport. In ship-board studies, important insights have come from using multiday quasi-Lagrangian drogue studies to quantify rates and stocks in a single water mass (e.g., Lomas et al. 2009; Taylor et al. 2012), but these lack contemporaneous measurements in adjacent water masses. To overcome these issues, a space-for-time approach can be used to help determine qualitative temporal changes in physical and biological/ecological interactions. The space-for-time approach can be used in a fixed, slowly varying flow feature where the spatial pattern reflects temporal succession along the flow path. While this approach has limitations, in upwelling systems like the CCE the space-for-time substitution has been shown to work well, specifically in the presence of mesoscale circulation features with time scales longer than the succession time scale of interest (reviewed by Pickett 1989).

We describe a study in the central CCE between Pt. Reyes and Monterey Bay, California aimed at examining the relative importance of physical transport and biological/ecological factors as drivers of phytoplankton taxonomic distribution during the productive upwelling season. A strong and persistent eddy-like feature determined spatial heterogeneity in phytoplankton biomass and provided a basis for evaluating offshore transport and vertical mixing using a multiday space-for-time approach. This specific physical feature sets up regularly during the upwelling season (Largier et al. 1993; Kaplan and Largier 2006; Halle and Largier 2011) and thus we expect that the processes inferred here are not isolated to the specific sampling period but are more general. Using changes in hydrography, nutrients, floristics, diatom productivity, and metatranscriptomics, the influence of advection, mixing, and physiology on phytoplankton composition was assessed.

## Methods

### Sampling

The "*DYE* labeling of di*atom* silica" (DYEatom) cruise examined spatial variability in diatom biomass during an upwelling event (R/V Pt. Sur; 27 June–05 July 2013). We targeted a range of bloom states using remote sensing (MODIS Level-2 product, NASA) and offshore currents derived from high frequency radar arrays (HFR, Kaplan and Largier 2006; Central and Northern California Ocean Observing System, www.cencoos.org). Specific station locations were determined by using satellite and HFR data together with the vessel's underway data acquisition system and by subsampling the uncontaminated seawater line to qualitatively assess diatom abundance and to define the bloom stage. All hydrocasts performed at each station were conducted in the immediate vicinity of a surface-tethered drogue (Brightwaters Instrument Corporation, Brightwaters, New York), deployed upon station occupation, to stay in the same water mass during repeat sampling; hydrocasts for biogenic silica production measurements (to quantify diatom productivity rates) and molecular work were separated by ~ 45 min.

Sampling was conducted just after local sunrise. The CTD rosette system was equipped with twelve 10-liter Niskin bottles, a Sea-Bird Electronics CTD, a Chelsea fluorometer, and a Biospherical Instruments photosynthetically active radiation (PAR) sensor. Mixed-layer depth was defined by a $> 0.125$ kg m$^{-3}$ increase in potential density ($\sigma_\theta$) relative to the surface. The magnitude of PAR just below the surface ($I_0$) was used to determine the depths at which PAR was 55%, 22%, 7%, and 1% of $I_0$. Water samples were collected at these depths to match neutral-density screened chambers placed in deck-board surface-water-cooled incubators. For all sampling, Niskin bottles were immediately drained into acid-cleaned 10-liter carboys, shaded and subsampled. CTD casts with no Niskin samples were conducted on a transect between Sta. 9 (offshore) and 10 (coastal) to define the physical structure of the eddy-like feature (Fig. 1).

### Biogenic silica production and kinetic experiments

Diatom productivity was quantified by measuring the rate of biogenic silica production using the radioisotope tracer $^{32}$Si; 300-mL samples received 260 Bq $^{32}Si(OH)_4$ (specific activity $> 40$ kBq $\mu$g Si$^{-1}$). Following isotope addition, bottles were placed in appropriate screened chambers within the deck-board incubator for 12 and/or 24 hours (depending on experiment type). After incubation, samples were filtered through 1.2 $\mu$m polycarbonate filters (Millipore), then processed and

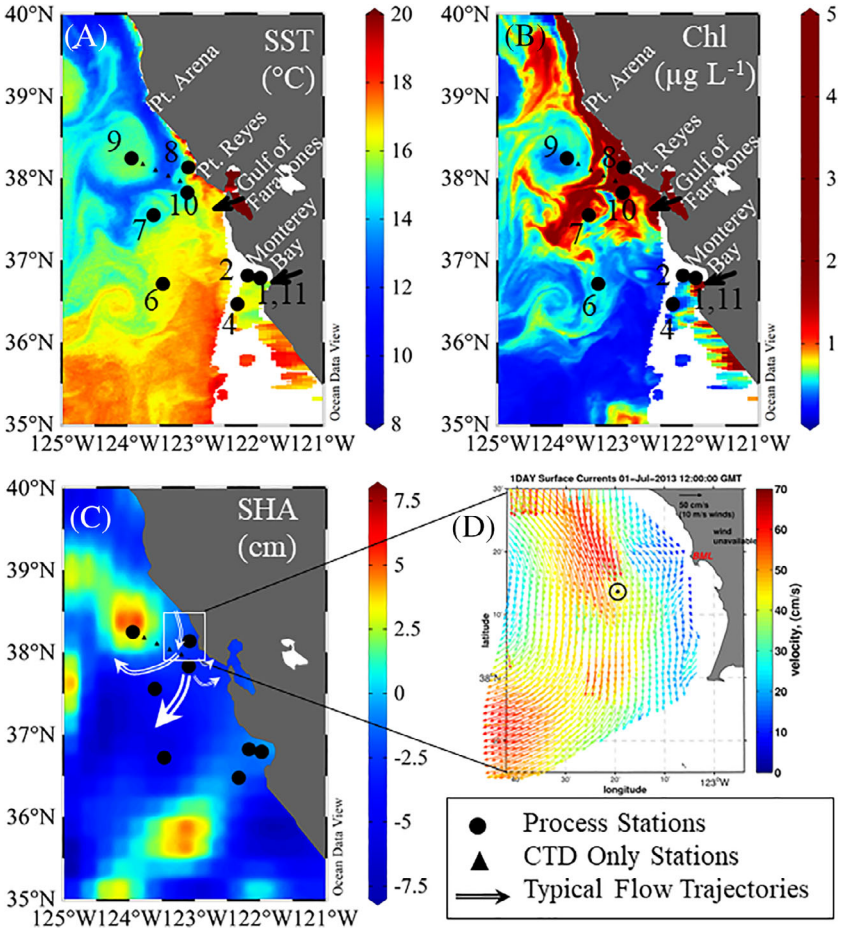


**Fig. 1.** Station locations (circles) and eddy transect line (small triangles) for the DYEatom cruise overlaid on Level-2 MODIS (A) sea-surface temperature (SST,°C) and (B) surface Chl concentration ($\mu$g $L^{-1}$) for 4 July 2013 (i.e., the closest cloud-free date to Pt. Reyes domain sampling 1–4 July 2013, oceancolor.gsfc.nasa.gov). (C) One-week Level-4 sea-surface height anomaly (SHA, cm) centered on 1 July 2013 (merged altimetry product available from Copernicus Marine Environment Monitoring Service; marine.copernicus.eu) and (D) 1-day surface currents (cm $s^{-1}$) from high-frequency radar array at the Bodega Ocean Observing Node on 1 July 2013-the date which sampling was started in the Pt. Reyes domain. For panel (C), typical flow patterns (Halle and Largier 2011) from Pt. Reyes are shown by arrows.

quantified as described in Krause et al. (2011). Gross production rates ($\rho$ in $\mu$mol Si $L^{-1}$ $d^{-1}$) were normalized to biogenic silica concentration ($bSiO_2$) to determine specific rates ($V_b$, $d^{-1}$), which is a proxy for diatom growth (Brzezinski and Phillips 1997). Two methods assessed whether the ambient [Si $(OH)_4$] limited diatom Si uptake, with both using the same $^{32}Si$ activity addition, incubation conditions and processing described above. First, eight samples collected from 55% $I_0$ were manipulated to make an eight-point silicic acid concentration gradient between ambient and + 18.0 $\mu$M [$Si(OH)_4$] (assumed to saturate Si uptake) and the radiotracer added to determine the concentration dependence of specific uptake rate. The concentration dependence of $V_b$ conforms to a rectangular hyperbola:

$$V_b = V_{max} \times [Si(OH)_4] \times (K_S + [Si(OH)_4])^{-1} \quad (1)$$

where $V_{max}$ is the maximum specific uptake rate and $K_S$ is half-saturation constant, that is, concentration where $V_b$ = 50% $V_{max}$. Data were fit to Eq. 1 using a nonlinear curve-fit algorithm (SigmaPlot 12.0). The second experiment type used only rates measured at ambient and + 18.0 $\mu$M [$Si(OH)_4$] but was conducted at multiple depths within the euphotic zone. The ratio of Si uptake at + 18 $\mu$M to that under ambient [$Si(OH)_4$] defines an enhancement (Enh) ratio and is a relative measure of the extent to which ambient [$Si(OH)_4$] restricts the rate of Si uptake. Under the assumption that the 18 $\mu$M [$Si(OH)_4$] additions saturate $Si(OH)_4$ uptake (i.e., approximate $V_{max}$ in Eq. 1), the inverse of Enh corresponds to $V_{amb}/V_{max}$ and represents the fraction of the maximum uptake rate supported by the ambient [$Si(OH)_4$] (Nelson et al. 2001). For example, an Enh ratio of 2 indicates that $V_{max}$ is twice the rate supported at the ambient [$Si(OH)_4$], (i.e., ambient [$Si(OH)_4$] limits uptake to 50% of its maximum). Enh ratios ~ 1 imply no substrate

limitation of Si uptake as additional $[Si(OH)_4]$ does not stimulate uptake. The Enh ratio can be described by rearranging Eq. 1:

$$\mathrm{Enh}\left(V_{\max} \times {V_b}^{-1}\right) = \left(K_S + \left[Si(OH)_4\right]_{amb}\right) \times {\left[Si(OH)_4\right]_{amb}}^{-1} \quad (2)$$

allowing estimates of $K_S$ as below

$$K_S = \left(\mathrm{Enh} \times \left[Si(OH)_4\right]_{amb}\right) - \left[Si(OH)_4\right]_{amb} \quad (3)$$

The Enh ratio is inverse of the Si stress metric ($V_{amb} : V_{max}$) used recently for a subset of these DYEatom cruise data (Kranzler et al. 2019); we choose the Enh ratio due to the larger dynamic range and because it can be reproduced easily by rearranging Eq. 1 to solve for $K_S$ (Eq. 3). The experimental uncertainties associated with this approach are discussed elsewhere (Nelson et al. 2001; Krause et al. 2012).

**Standing stock measurements**

Particulate and nutrient stocks were sampled following standard protocols. Water sampled for inorganic nutrients was syringe-filtered (0.6-$\mu$m pore polycarbonate filter) into plastic vials, immediately frozen at −20°C, and quantified onshore using an autoanalyzer (Brzezinski and Washburn 2011); detection limits for nitrate + nitrite (N + N) and silicic acid (Si $(OH)_4$) were 0.1 $\mu$M and 0.2 $\mu$M, respectively (phosphate was analyzed but is not discussed). Seawater (200–350 mL) was filtered through a cellulose filter (0.45-$\mu$m pore) for determination of Chlorophyll *a* (Chl *a*) using a 90% acetone extraction and acidification technique (Brzezinski and Washburn 2011). For $bSiO_2$ concentration, seawater (600 mL) was filtered through a 1.2-$\mu$m pore polycarbonate filter, immediately frozen, and analyzed using a modified alkaline digestion method (Krause et al. 2012). Biomass for metatranscriptomic analysis was collected onto 1.2-$\mu$m pore polycarbonate filters by filtration at < 0.03 MPa for no longer than 15 min, snap frozen in liquid $N_2$, and stored at −80°C.

**RNA extraction, sequencing, and assembly**

Details of 18S and metatranscriptome assembly and analysis are published elsewhere (Kranzler et al. 2019), but are briefly described here. One billion copies of each of two commercially available RNA standards (purified RNA transcripts) were added to each filter (#1, #8 ArrayControl™ Spots and Spikes, ThermoFisher Scientific, with polyA tails). RNA was extracted using TRIzol reagent (Life Technologies) with cDNA prepared using the SuperScript III First Strand Synthesis system with random hexamers (Life Technologies), then amplified using an AccuPrime PCR system kit (Life Technologies). Amplification was done as follows: initial denaturation at 95°C for 2 min and 30 cycles of 95°C for 20 s, 56°C for 30 s, and 72°C for 5 min. Products (2 $\mu$L of sample; 5 $\mu$L of NTC) were run on a 1% agarose gel, cleaned with Ampure XP beads (Beckman Coulter), and resuspended in 25 $\mu$L of Qiagen (Hilden, Germany) elution buffer. Samples were visualized on an agarose gel and quantified using the PicoGreen Quant-IT assay (Life Technologies); 45 ng of 18S amplicons were pooled for 454 pyrosequencing.

18S ribosomal RNAs (rRNAs) were sequenced using 454 pyrosequencing. TAReuk454FWD1 (5′-CCAGCASCYGCG GTAATTCC-3′) and TAReukREV3 (5′-ACTTTCGTTCTTGA TYRA-3′) (Stoeck et al. 2010) were used to target a 500 bp region of the v4 region of the 18S rRNA. FLX Titanium adapters (A-adapter sequence: 5′-127 CCATCTCATCCCTGCG TGTCTCCGACTCAG-3′; B-adapter sequence: 5′-128 CCTA TCCCCTGTGTGCCTTGGCAGTCTCAG-3′) and 10 bp multiplex identifier barcodes were used for multiplexed sequencing.

Library QC, emPCR, enrichment, and 454 sequencing were done according to the manufacturer's protocol (Roche Diagnostics; Risch-Rotkreuz, Switzerland) with the following modifications: KAPA Biosystems Library Quantification Kit for qPCR was used to estimate the number of molecules needed for emPCR, automation (BioMek FX) was used to "break" the emulsions after emPCR, and butanol was used to for ease of handling during the breaking process. Bead enrichment was automated by using Roche's REM (Robotic Enrichment Module).

18S rRNA 454 reads were demultiplexed using Roche/454's Sfffile utility and converted from standard flowgram to FASTA format using sff2fastq, followed by primer removal, quality control, trimming, and dereplication. Chimeric sequences were removed using USEARCH (Edgar 2010), reads were trimmed to a quality score of 10 over a 2-base window, operational taxonomic units were clustered using SWARM (Mahé et al. 2015) and classified using FASTA36 from the FASTA package. Taxonomic annotations were assigned by using GLSEARCH36 (Pearson 2016) with a modified PR2 database with updates from Tara Oceans W2 (De Vargas et al. 2015).

Metatranscriptome libraries were constructed using 500 ng of total RNA and a TruSeq RNA Sample Preparation Kit (Illumina), following the Low-Throughput protocol. The mean size of the final libraries was confirmed to be between 359 and 420 base pairs (bp) using an Agilent Bioanalyzer 2100. Libraries were paired-end sequenced (2 × 150 bp) on the Illumina HiSeq platform.

Reads were trimmed to remove primers and areas of low sequence quality (i.e., < 30 bp long and a quality score < 33). Illumina reads were paired. rRNA reads were removed using Ribopicker v.0.4.3 (Schmieder et al. 2011). Large fraction reads were assembled by library, then overall, using CLC Genomics Workbench 9.5.3. Ab initio ORF prediction was performed with FragGeneScan (Rho et al. 2010). ORFs were screened for contamination in the form of rRNA, ITS, and primers. ORFs with closer homology to a known organelle gene than that of a nuclear gene in the same reference organism were filtered.

ORFs were annotated via BLASTP (Altschul et al. 1990) alignment ($e$ value $> 1e^{-3}$) to a comprehensive protein

database, *phyloDB*, as well as screened for function de-novo by assigning Pfams, TIGRfams, and transmembrane tmHMMs with hmmer 3.0 (http://hmmer.org/) (Sonnhammer et al. 1998). PhyloDB 1.076 consists of 24509327 peptides from 19962 viral, 230 archaeal, 4910 bacterial, and 894 eukaryotic taxa. It includes peptides from KEGG, GenBank, JGI, ENSEMBL, CAMERA, and various other repositories, as well as the 410 taxa of the Marine Microbial Eukaryotic Transcriptome Sequencing Project (Caron et al. 2017). Taxonomic annotation of ORFs was also conducted via a BLASTP to phyloDB.

Added RNA spikes were used to estimate the absolute number of RNA copies per liter of seawater for reads within each library. Reads per bp for ORFs of interest were divided by spike reads recovered per bp per copy spike added per liter seawater for each library. For ORFs > 1000 bp, recovery of spike 8 (2000 bp without tail) was used. For ORFs < 1000 bp, spike 1 (750 bp without tail) was used. Reads per kilobase (RPK) normalization was used to assess the relative transcriptional activity of the major eukaryotic phytoplankton groups. The fraction of transcriptional activity for each taxonomic group was calculated by dividing the total RPK for each group (diatoms, dinoflagellates, haptophytes, and chlorophytes) by the total RPK for all groups. Genes associated specifically with exponential growth spanning a range of pathways, defined in Ashworth et al. (2013), were identified by KO among the four phytoplankton groups (Table S1). These genes are not expressed during stationary growth phase and represent genes involved in light capture, photosynthesis, carbon fixation, and oxidative phosphorylation providing a range of genes involved in distinct biochemical pathways associated with exponential growth (hereafter referred to as "exponential growth" genes).

## Results

### Hydrography and circulation

Stations were differentiated using hydrographic data. Newly upwelled waters exhibited high euphotic-zone potential density ($\sigma_\theta$), most common toward the coast. Only Sta. 6 and 9 had low euphotic zone density: $\sigma_\theta < 25.1$ kg m$^{-3}$ (Table 1). Compared with the average euphotic-zone $\sigma_\theta$ for other stations ($25.64 \pm 0.12$ kg m$^{-3}$), the average $\sigma_\theta$ at Sta. 6 and 9 were 4.7 and 8.5 standard deviations lower, respectively. Thus, Sta. 6 and 9 were largely influenced by offshore waters, whereas $\sigma_\theta$ among other stations varied little (despite the variable bottom depths) and was characteristic of upwelled waters. This $\sigma_\theta$ criterion was robust for other metrics, as average euphotic Chl *a* in these two offshore stations (Sta. 6 and 9) were < 1 $\mu$g L$^{-1}$, whereas the average euphotic Chl *a* among coastal water stations ranged from 3.9 to 18.0 $\mu$g L$^{-1}$ (Table 1). Given the influence of an eddy-like feature in the northern sampling domain, coastal stations are further differentiated by region: Monterey Bay or Pt. Reyes (Table 1). Hereafter, we will refer to stations by each coastal region (Monterey Bay, Pt. Reyes) or offshore (Table 1).

Typical early-summer conditions were observed. Strong gradients in [Chl *a*] between coastal (high) and offshore (low) waters were negatively correlated with SST, suggestive of upwelling (Fig. 1A,B). Prior to the cruise, upwelling-favorable alongshore winds (i.e., northerly) were concurrent with a lowering of SST (Fig. 2A,B). In the days before Sta. 1 was occupied, alongshore wind reversed near Bodega Bay and reduced off Monterey Bay (Fig. 2A). This relaxation led to increased SST in both regions (Fig. 2B). However, from 28 June through the end of the cruise, upwelling-favorable winds persisted. Remote-sensing data (SST, [Chl *a*], altimetry, currents; Fig. 1) confirm that recently upwelled water was mostly advected offshore with little water advected alongshore or into the Gulf of the Farallones (Fig. 1). Overall, Monterey Bay waters were saltier than Pt. Reyes (Fig. 2C); the lowest salinities were observed in the euphotic zone offshore at Sta. 6 and 9 where temperatures exceeded 12°C (Fig. 2C). Temperature-salinity data from Sta. 10, downstream of Sta. 8, show a slight freshening and warming of the surface waters during transit (Fig. 2C), suggesting that lower salinity water from the Gulf of Farallones was entrained into the high-salinity upwelled water in the vicinity of Pt. Reyes.

Remote sensing and ancillary data confirmed the presence of a mesoscale eddy-like feature offshore Pt. Reyes (Fig. 1A–C), with Sta. 9 being in the warm, low-Chl core, confirmed by observations of near-zero current velocity on the shipboard ADCP. Sta. 9 had lower surface potential density and salinity (Fig. 2D) than at the feature's edge where colder upwelled water was being actively advected offshore and around the periphery (Fig. 1D). MODIS data (Fig. 1A,B) show a clear distinction between low-Chl water in the core of the eddy (Sta. 9) and high-Chl water nearshore and in the Gulf of the Farallones (Sta. 10; Fig. 2D). During upwelling, flow past Pt. Reyes is southward, turning offshore and advecting upwelled waters southwestward (Fig. 1C, Halle and Largier 2011). In the presence of the eddy-like feature, offshore transport is increased, as seen in MODIS images (Fig. 1A,B) and surface-current (Fig. 1D) data. This feature is common locally (Largier et al. 1993), and starts as a "recirculation" meander, which can develop into a closed eddy-like feature (Halle and Largier 2011). At the time of our study, the eddy-like feature was not completely closed, as high [Chl *a*] water from the coastal zone was being mixed with low [Chl *a*] water from further offshore (Fig. 1B). The magnitude of maximum flow, 50–70 cm s$^{-1}$ (Fig. 1D), is similar to current velocities for this feature observed in previous years (Largier et al. 1993; Halle and Largier 2011) and provided the physical forcing necessary to evaluate spatial (i.e., temporal) trends within a space-for-time framework.

### Nutrient and particulate standing stocks

Upwelling-favorable winds increased surface nutrient concentrations at some stations (Fig. 3A,B). At most stations, the

**Table 1.** Properties and rates among stations. Euphotic zone (EZ) and mixed layer (ML) depth, average temperature (temp.), salinity (Sal.), potential density ($\sigma_\theta$), nitrate + nitrite [N + N], and chlorophyll *a* [Chl *a*] in the EZ. For Si-related measurements, EZ average (Ave) and integrated ($\int$) values are reported for dissolved silicic acid [$Si(OH)_4$], biogenic silica [$bSiO_2$], daily $bSiO_2$ production ($\rho$). Also reported, is the relative abundance of different diatom genera, based on %18S rRNA, among stations and light depths within the EZ (noted as percentage relative to irradiance just below the surface, % $I_0$). As described in the methods, domains are subdivided by coastal region MB (Monterey Bay), PR (Pt. Reyes), and offshore stations (OS).

| | | | | | | | [$Si(OH)_4$] | | [$bSiO_2$] | | 24-h $\rho$ | | %18S rRNA for dominant diatom genera, relative to the total, by light depth (% $I_0$) |
|---|---|---|---|---|---|---|---|---|---|---|---|---|---|
| Domain | Station | EZ (m) | ML (m) | Ave temp., Sal., $\sigma_\theta$ | Ave. [N+N] ($\mu$M) | Ave [Chl a] ($\mu$g $L^{-1}$) | Ave ($\mu$M) | $\int$(mmol $m^{-2}$) | Ave ($\mu$mol $L^{-1}$) | $\int$(mmol $m^{-2}$) | Ave ($\mu$mol $L^{-1}$ $d^{-1}$) | $\int$(mmol $m^{-2}$ $d^{-1}$) | |
| MB (coast) | 1 | 10 | 7 | 11.92°C<br>33.86‰<br>25.71 kg $m^{-3}$ | 4.6 | 18.0 | 10.6 | 89 | 8.4 | 80 | 2.9 | 31 | — |
| | 2 | 18 | 23 | 11.52°C<br>33.87‰<br>25.80 kg $m^{-3}$ | 9.3 | 8.1 | 11.7 | 199 | 5.6 | 96 | 2.5 | 42 | 93% *Pseudo-nitzschia* (55%)<br>95% *Pseudo-nitzschia* (22%)<br>91% *Pseudo-nitzschia* (1%) |
| | 4 | 15 | 16 | 12.33°C<br>33.80‰<br>25.60 kg $m^{-3}$ | 2.4 | 11.6 | 3.5 | 47 | 5.7 | 82 | 1.5 | 23 | 95% *Pseudo-nitzschia* (55%)<br>90% *Pseudo-nitzschia* (22%)<br>91% *Pseudo-nitzschia* (1%) |
| | 11 | 15 | 11 | 12.09°C<br>33.82‰<br>25.66 kg $m^{-3}$ | 8.4 | 10.0 | 10.5 | 136 | 4.3 | 68 | 3.8[a] | 59[a] | 92% *Pseudo-nitzschia* (55%)<br>93% *Pseudo-nitzschia* (22%)<br>95% *Pseudo-nitzschia* (1%) |
| PR (coast) | 7 | 14 | 18 | 11.75°C<br>33.53‰<br>25.49 kg $m^{-3}$ | 2.1 | 3.9 | 2.0 | 27 | 8.2 | 108 | 1.5 | 20 | 52% *Thalassiosira* (55%)<br>33% *Thalassiosira* (22%)<br>34% *Pseudo-nitzschia* (1%) |
| | 8 | 11 | 7 | 11.45°C<br>33.76‰<br>25.73 kg $m^{-3}$ | 3.5 | 7.5 | 7.3 | 68 | 14.2 | 155 | 2.4 | 23 | 30% *Chaetoceros* (55%)<br>25% *Thalassiosira* (22%)<br>61% *Chaetoceros* (1%) |
| | 10 | 10 | 10 | 12.48°C<br>33.70‰<br>25.49 kg $m^{-3}$ | 0.5 | 4.2 | 1.3 | 12 | 12.2 | 101 | 0.8 | 8.0 | 19% *Thalassiosira* (55%)<br>20% *Thalassiosira* (22%)<br>34% *Thalassiosira* (1%) |
| OS | 6 | 35 | 26 | 13.88°C<br>33.54‰<br>25.08 kg $m^{-3}$ | 6.3 | 0.9 | 8.3 | 272 | 1.0 | 33 | 0.4 | 11 | 60% *Pseudo-nitzschia* (55%)<br>52% *Pseudo-nitzschia* (22%)<br>53% *Pseudo-nitzschia* (1%) |
| | 9 | 55 | 27 | 13.62°C<br>32.88‰<br>24.62 kg $m^{-3}$ | 2.1 | 0.3 | 5.3 | 345 | 0.2 | 14 | 0.1 | 2.8 | 49% *Thalassiosira* (55%)<br>55% *Thalassiosira* (22%)<br>50% *Pseudo-nitzschia* (1%) |

*12 (not 24) hour incubation.

nitrate plus nitrite concentration ([N + N]) and [$Si(OH)_4$] in the surface waters showed drawdown relative to deeper waters and surface concentrations for both were < 2 $\mu$M in the Pt. Reyes domain (Fig. 3A,B). Nutrient concentrations increased sharply below the euphotic zone to ~ 20 $\mu$M for [N + N] and to 20–30 $\mu$M for [$Si(OH)_4$] (Table S2). Given the space-for-time framework in the Pt. Reyes domain, nutrients within the euphotic zone were most depleted in the coastal stations and increased during transit offshore. This spatial trend co-occurred with increases in the mixed-layer depth between the Pt. Reyes stations (7, 8, and 10) and the two offshore stations (Sta. 6 and 9; Table 1).

At stations with reduced surface nutrients, [Chl *a*] was high near-surface (8–20 $\mu g\ L^{-1}$, Fig. 3C) and typically declined with increasing depth (Table S2). [$bSiO_2$] in the euphotic zone showed similar trends as [Chl *a*], with a maximum at or near the surface; the highest concentration, 16 $\mu mol\ L^{-1}$, was observed in the Pt. Reyes domain (Fig. 3D). Integrated $bSiO_2$ in the euphotic zone spanned an order of magnitude 14–155 mmol Si $m^{-2}$ (Table 1). At some stations, $\int bSiO_2$ exceeded $\int Si(OH)_4$ (e.g., Monterey Sta. 4, Pt. Reyes Sta. 7, 8, and 10; Table 1), suggesting a majority of $Si(OH)_4$ had been converted to diatom biomass. Spatial (i.e., temporal) differences between newly upwelled water at Pt. Reyes and older water at offshore stations, shows that biomass (both Chl *a* and $bSiO_2$) declined up to an order of magnitude as waters were advected offshore over a few days.

**Biogenic silica production and diatom nutrient stress**

Diatom productivity rates fluctuated among stations. In Monterey Bay, $\rho$ was highest in the upper 10 m (~ 4 $\mu mol\ Si\ L^{-1}\ d^{-1}$, Fig. 3E) and rapidly declined with depth toward ~ 0 at the base of the euphotic zone (Table S2). Among the Pt. Reyes domain stations, the maximum value of $\rho$ also occurred in the upper 10 m, with the highest value observed at 8 m at Sta. 8 (~ 6 $\mu mol\ Si\ L^{-1}\ d^{-1}$). Productivity rates at offshore stations (Sta. 6 and 9) were low and more typical of rates observed in the deep-water southern CCE domain (Krause et al. 2015). Specific rates, $V_b$, at the 55% $I_0$ irradiance depth showed significant spatial variability: 0.5–0.9 $d^{-1}$ and < 0.1–0.4 $d^{-1}$ in the Monterey Bay and Pt. Reyes domain, respectively (Fig. 3F). Specific rates were higher in the offshore stations, pointing to sustained diatom productivity. The euphotic-zone integrated $\rho$ showed a similar variability as $bSiO_2$, 2.8–59 mmol Si $m^{-2}\ d^{-1}$ (Table 1). The highest $\int\rho$ was observed in Monterey Bay, although these were on the lower end of rates observed in other years earlier in the upwelling season (Brzezinski et al. 1997, 2003).

Ambient [$Si(OH)_4$] limited diatom $bSiO_2$ production at most stations. Eight-point kinetic experiments showed hyperbolic responses (Fig. 4A). $V_{max}$ ranged from $0.01 \pm 0.00\ h^{-1}$ (Sta. 8) to $0.05 \pm 0.00\ h^{-1}$ (Sta. 7 and 11 rates nearly identical). $K_S$ were similar between Sta. 7 ($2.5 \pm 0.6$ $\mu$M) and 8 ($2.7 \pm 0.8$ $\mu$M), but lower at Sta. 11 in Monterey Bay, $0.8 \pm 0.2$ $\mu$M (Fig. 4A). The Enh ratios were 2.5, 6.7, and 1.3 for Sta. 7, 8, and 11, respectively. Among two-point experiments, significant Enh ratios (i.e., above experimental error) were observed in ~ 70% of incubations (Fig. 4B). When [$Si(OH)_4$] < 4 $\mu$M, the Enh ratio increased from ~ 1 (i.e., no limitation) to nearly 12 (Fig. 4B) implying that $V_b$ was limited to < 10% of $V_{max}$ (i.e., $Enh^{-1}$). The average $K_S$ calculated using Eq. 2 and Enh data from all stations, i.e., among assemblages, was $4.4 \pm 0.2$ $\mu$M (Fig. 4B). Given the ambient [$Si(OH)_4$] observed, 49% of the diatom assemblages sampled were taking up $Si(OH)_4$ at a rate less than half of $V_{max}$ and corresponding to Enh > 2. Transit offshore, driven largely by the eddy-like feature, co-occurred with a reduction in limitation by Si; upper-euphotic zone Enh decreased from $7.8 \pm 2.4$ among the Pt. Reyes stations (7, 8, and 10) to $1.3 \pm 0.1$ among the offshore stations (6 and 9).

Other forms of nutrient stress may have also been present. For macronutrients, a previous study demonstrated that these communities during the DYEatom cruise were primarily limited for Si despite concomitant low nitrate availability (Kranzler et al. 2019). Given these authors made a relative comparison, N limitation could have been present at all stations, i.e., no station more limited relative to another, but this is unlikely since average [N + N] was high at multiple stations (Table 1). However, the metatranscriptomic data indicated the presence of iron stress. The expression of the iron-responsive ISIP gene family in diatoms was higher, albeit variable, in Monterey Bay compared to Pt. Reyes (Fig. 4C, Table S3). Low expression was also observed in Sta. 9 within the eddy-like feature, while the median expression of ISIP was higher in offshore Sta. 6. This suggests that as waters transited from Pt. Reyes toward offshore sites, there was little or no change in ISIP expression (Sta. 9) or an increase in ISIP expression over time (Sta. 6).

**Community composition and diatom activity**

Diatoms dominated 18S rRNA reads (> 50% of the total) in all Monterey Bay stations and Sta. 7 and 8 in Pt. Reyes domains (Fig. 5A; Kranzler et al. 2019). The offshore stations (Sta. 6, 9) had more diverse assemblages with reads associated with dinoflagellates and haptophytes representing 5–30% and 0–18% of the total, respectively (Kranzler et al. 2019). Among diatoms, *Pseudo-nitzschia* was the most abundant genus in the upper euphotic zone of the Monterey Bay domain and offshore at Sta. 6, while the Pt. Reyes domain was more diverse with representation by *Chaetoceros*, *Thalassiosira*, and other minor constituents (Table 1). If offshore waters at Sta. 6 originated from high-Chl *a* coastal water (e.g., Pt. Reyes), then there was succession during the advective transit, from *Chaetoceros* and *Thalassiosira* dominated assemblages (Pt. Reyes stations, offshore Sta. 9) to *Pseudo-nitzschia* (offshore Sta. 6) associated.

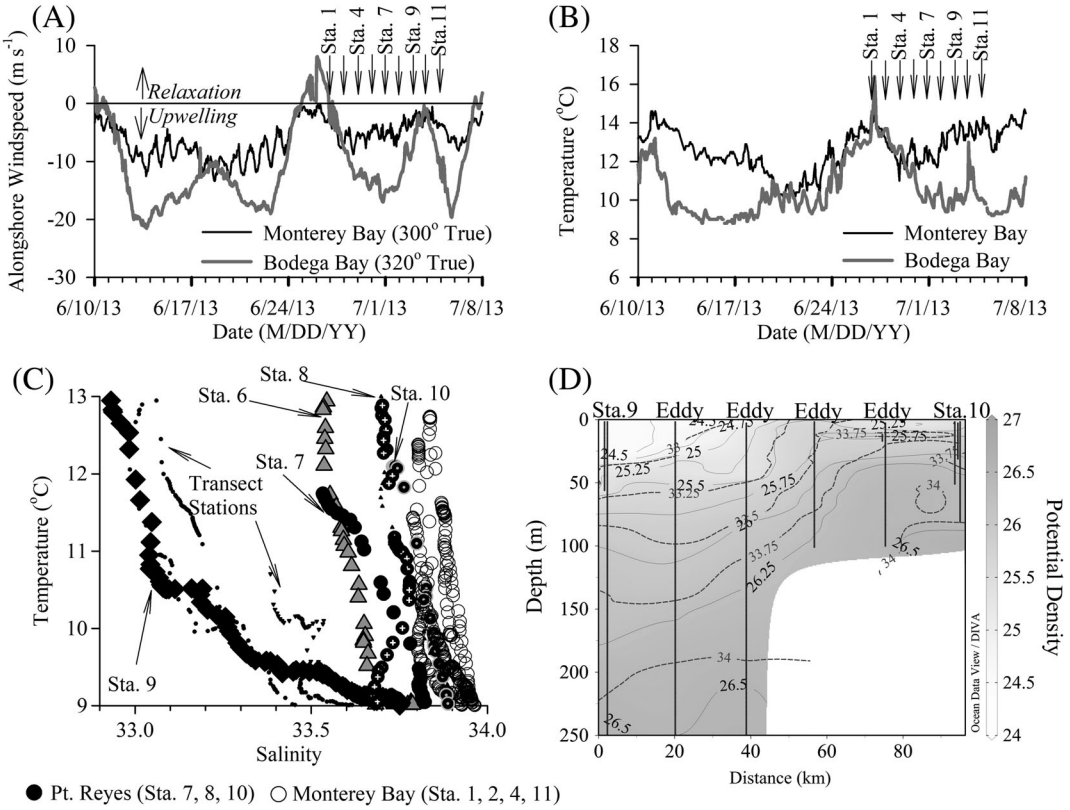


**Fig. 2.** (A) Along shore wind speed (m s$^{-1}$) and temperature (°C) for Buoys 46092 (Monterey Bay) and 46013 (Bodega Bay) from 10 June through 8 July 2013 (data from ndbc.noaa.gov). Station dates are located above each panel. Wind speed was aligned to the 300° and 320° true and data was smoothed using a 36-h function where $[(t_{-18})/2 + (t_{-17}) + \ldots + (t) + \ldots + (t_{17}) + (t_{18})/2]/36$, where $t_{-x}$ and $t_{+x}$ represent the means calculated $x$ hours before and after time $t$, respectively, similar 36-h filters have been used in this region (Largier et al. 2006). (C) Temperature (°C) vs. salinity for Pt. Reyes stations (St. 7 filled circles, St. 8 filled circles with cross hairs, St. 10 filled with gray edge), Monterey Bay stations (open circles), Sta. 9 (filled diamonds), Sta. 6 (gray triangles), and eddy transect (small triangles in Fig. 1 and panel [D] "Eddy" stations). (D) Potential density ($\sigma$, kg m$^{-3}$) section plot with salinity overlay (dashed contours) for eddy transect between Sta. 9 and 10.

Metatranscriptomic analysis was used to determine the relative transcriptional activity of the major eukaryotic phytoplankton groups. Based on the total normalized transcript abundance, diatoms were the most transcriptionally active members of the community in the upper euphotic zone at all stations (40–84%, Fig. 5B), followed by dinoflagellates (7–46%, Fig. 5B). Haptophyte (2–10%) and chlorophyte (1–10%) transcripts made up a smaller fraction of the total community (Fig. 5B). Diatoms were negatively correlated with the other three groups: dinoflagellates (Pearson $r$ = –0.99, $n$ = 24, $p < 0.0001$; Fig. 5C open symbols), haptophytes ($r$ = –0.98, $n$ = 24, $p < 0.0001$), chlorophytes ($r$ = –0.56, $n$ = 24, $p$ = 0.005). The non-diatom groups were all positively and significantly correlated to one another (Pearson $r$ range: 0.45–0.95, $p$-value range: < 0.0001–0.03). Given that previous studies have demonstrated total transcriptional activity is a reasonable proxy for numerical abundance for both diatoms and dinoflagellates (Alexander et al. 2015; Lampe et al. 2018; Zhang et al. 2019), these data suggest that diatoms and dinoflagellates were the dominant members of the eukaryotic phytoplankton community. Their strong negative correlation highlights the ecological niche differences between diatoms and dinoflagellates.

Although transcript abundance can serve as a reasonable proxy for abundance, it alone does not indicate growth or productivity. However, we reasoned that a subset of genes known to be associated with growth and photosynthesis can provide a measure of "activity." In a global survey of genetic data collected during the *Tara* Oceans, diatom-specific genes associated with photosynthesis and carbon fixation were strongly correlated with net primary productivity (Carradec et al. 2018). In addition, genes associated with cellular biochemical pathways, such as photosynthesis, carbon fixation, and the pentose phosphate pathway were found to specifically be up-regulated during exponential growth (Ashworth et al. 2013). Thus, we explored the expression of "exponential growth" genes (Table S1) in our metatranscriptome data as proxies for diatom growth and activity. Contigs associated with diatoms dominated "exponential growth" transcripts at nearly all stations (Fig. 5C, filled squares). Among the 24 metatranscriptome

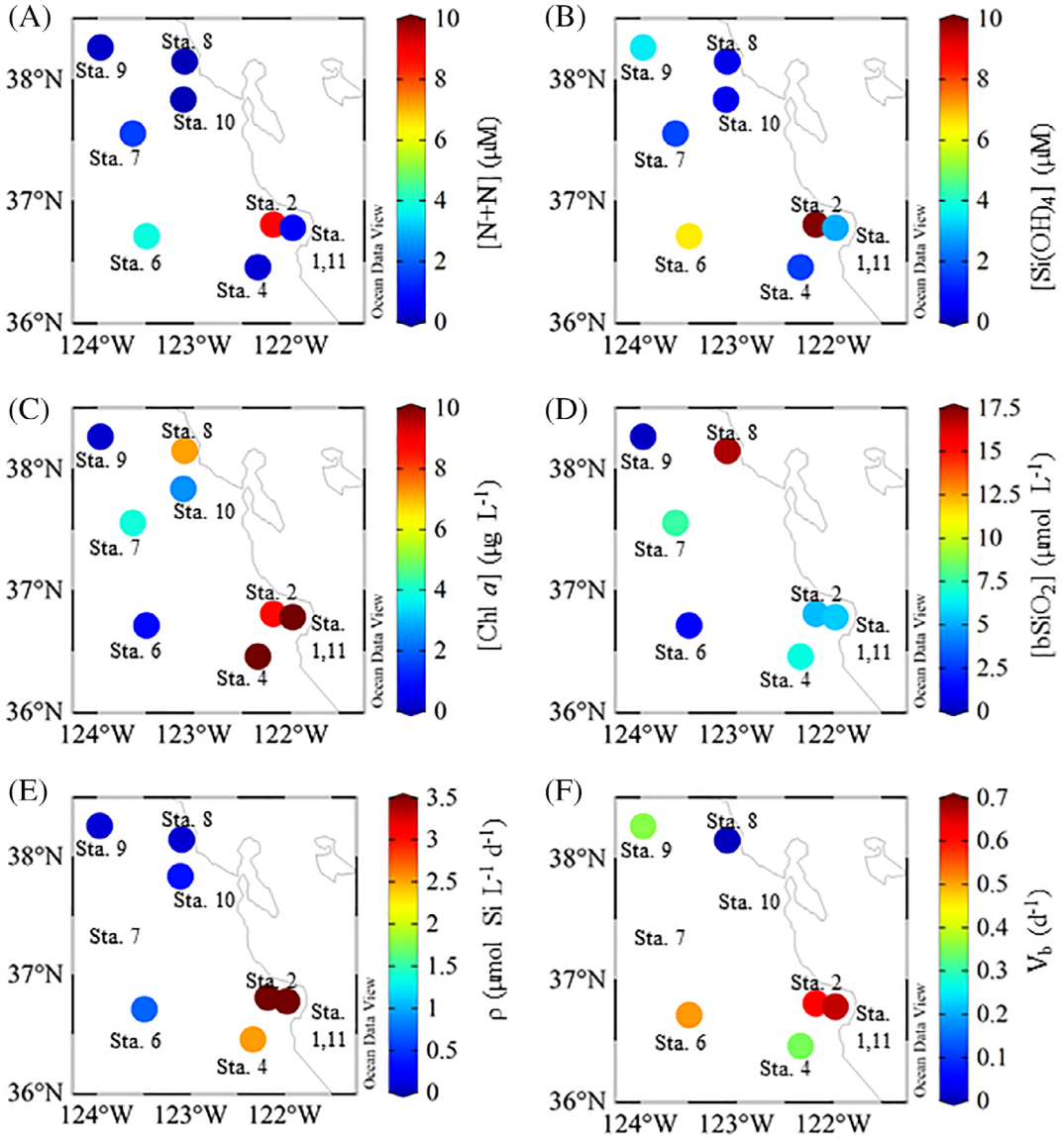


**Fig. 3.** Surface map of (A) nitrate + nitrite [N + N] ($\mu$M), (B) silicic acid [$Si(OH)_4$] ($\mu$M), (C) chlorophyll *a* [Chl *a*] ($\mu$g $L^{-1}$), biogenic silica (D) stock [$bSiO_2$] ($\mu$mol $L^{-1}$), (E) rate of production $\rho$ ($\mu$mol Si $L^{-1}$ $d^{-1}$), and (F) biomass-specific production rate $V_b$ ($d^{-1}$) among all stations (labeled). All data is from the 55% $I_0$ isolume (note: No [$bSiO_2$] data are available for Sta. 10 at this light depth, no 24-h $\rho$ or $V_b$ for Sta. 7).

samples examined across all stations, there were only two where the contribution of diatoms to the "exponential growth" contigs was less than the percent contribution to total transcripts (Sta. 7 55% $I_0$ and 1% $I_0$, i.e., two points below 1 : 1 line, Fig. 5C). Thus, even when diatoms' contribution to the total transcripts were low (e.g., Sta. 6, 9; Fig. 5B), they were disproportionally active (i.e., higher contribution to "exponential growth" genes) in the upper euphotic zone (Fig. 5C). This same disproportionate activity in "exponential growth" genes was observed for haptophytes, but not dinoflagellates (Table S1); however, unlike diatoms and dinoflagellates, haptophytes never represented a majority of either total transcripts or contribution to "exponential growth" genes. The remainder of the manuscript focuses on the general dynamic between diatoms and dinoflagellates within the space-for-time framework (i.e., advection of Pt. Reyes domain water offshore).

### Euphotic zone diatom activity and inshore-to-offshore changes in the Pt. Reyes domain

Changes in diatom "exponential growth" gene abundance and phytoplankton biomass followed changes in hydrography between inshore stations in the Pt. Reyes domain (Sta. 7, 8, and 10) toward offshore Sta. 6 and 9 (Fig. 2C). Given a space-for-time assumption, offshore stations 6 and 9 represent aged waters (e.g., Fig. 1C) that originated inshore in the Pt. Reyes domain. Sta. 6 is a typical destination for coastal upwelled water (Halle and Largier 2011) while Sta. 9 is characteristic of the core of the eddy-like feature (Fig. 1). Salinity decreased

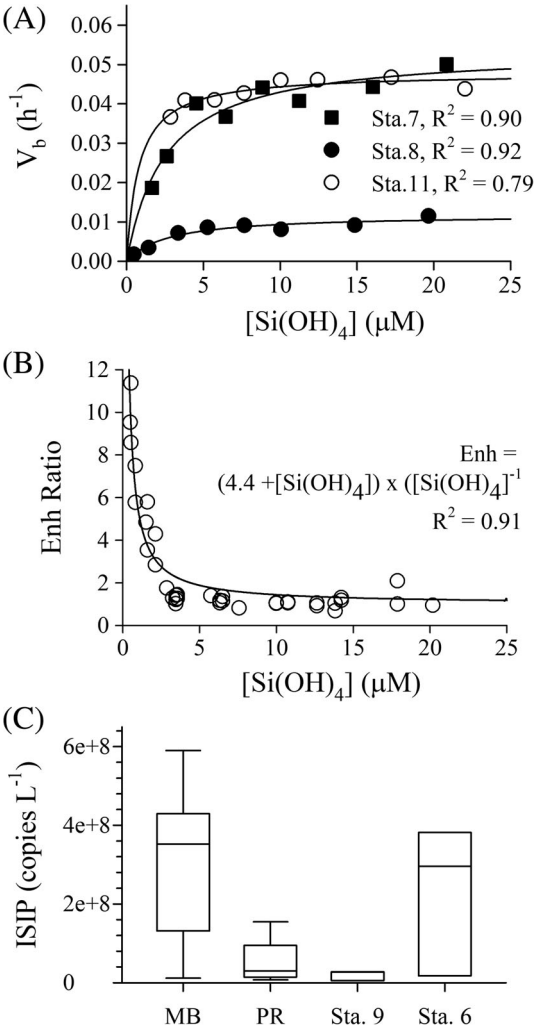


**Fig. 4.** Nutrient limitation metrics. (A) $V_b$ ($h^{-1}$) as a function of silicic acid concentration ($\mu$M) for experiments conducted at Sta. 7 ($R^2$ = 0.90, $p < 0.001$), 8 ($R^2$ = 0.92, $p < 0.001$), and 11 ($R^2$ = 0.79, $p < 0.002$). (B) Enh ratio as a function of ambient [Si(OH)$_4$] for all incubations fitted to Eq. 2 ($R^2$ = 0.91, $p < 0.001$). Nonlinear regressions were fit using SigmaPlot 12.0. (C) Box plot of ISIP (copies $L^{-1}$) among Monterey Bay (MB), Pt. Reyes (PR), and Sta. 6, 9.

between coastal and offshore stations (Fig. 2C), indicating the mixing in of low-salinity waters from the Gulf of Farallones and/or offshore surface waters. Thus, salinity indexes the offshore flow and changes in both gene abundance (e.g., total diatom transcripts, Pearson $r$ = 0.72, $p < 0.0001$) and phytoplankton biomass (e.g., Chl *a*, Pearson $r$ = 0.73, $p < 0.0001$) were both positively and significantly correlated with salinity (Fig. 6).

Among all depths, the proportional change in total diatom transcripts along the Sta. 9 trajectory was 45% for each 1 part-per-thousand salinity change ($R^2$ = 0.40, $p$ = 0.033, Fig. 6A); this change was lower when only "exponential growth" genes were considered (34%, $R^2$ = 0.53, $p$ = 0.010, Fig. 6B). For the inshore-to-offshore trajectory from Pt. Reyes toward Sta. 6, the change in total diatom transcripts was 36% per 1 part per thousand but the slope was not statistically significant ($R^2$ = 0.03; $p$ = NS). When considering only the diatom contribution to "exponential growth" genes, there was no relationship with salinity when considering Sta. 6 as an end member ($R^2$ = 0.18; $p$ = NS, Fig. 6B). Associated with these salinity relationships are trends with increasing mixed layer depth, which increased at the offshore stations (Table 1). Total diatom transcripts (Fig. 6E) and diatom contribution to "exponential growth" genes (Fig. 6F) were thus inversely related to mixed layer depth, implying decreased diatom biomass and activity in a deeper mixed layer. Unlike with salinity, the slopes were nearly identical between trajectories and both were statistically significant (Fig. 6F).

Other factors varied with salinity. When examining metrics of nutrient limitation, the Enh factor declined with reduced salinity in both trajectories, Sta. 9 and 6, with the linear slopes both being significantly different from zero (Fig. 6C). These same declining trends with lower salinity were observed for [Chl *a*] ($R^2$ = 0.61, $p$ = 0.003 and $R^2$ = 0.41, $p$ = 0.024 for Sta. 9 and 6 trajectories, respectively; Fig. 6D) but there were no significant relationships between salinity and nutrient concentration (data not shown).

## Discussion

Phytoplankton succession is governed by physiological traits modulated by changes in the abiotic environment over time. Trait-based modeling has provided new insights to explain distributions in biogeochemical parameters and predict how they might change in the future (Lomas et al. 2014; Teng et al. 2014). Typically, these successional patterns are driven by vertical (e.g., light, nutrients) and horizontal (e.g., temperature/salinity, nutrients) gradients which develop over weeks to months. However, rapid changes in phytoplankton taxonomic composition can also arise through mixing of previously discrete phytoplankton assemblages. Understanding how physics, physiology, and ecology combine to affect phytoplankton dynamics is important (Behrenfeld and Boss 2014 and references therein).

The CCE has well-described phytoplankton succession events during upwelling season. During the "Wind Events and Shelf Transport" program in the Pt. Reyes domain (Largier et al. 2006), large phytoplankton cells (mainly diatoms) were observed to dominate early and mid-phases of upwelling, and typically drive high Chl a near the coast (Lassiter et al. 2006; Wilkerson et al. 2006). Smaller flagellates were observed to dominate late upwelling phases and offshore regions (Lassiter et al. 2006; Wilkerson et al. 2006). These general successional trends in response to upwelling phases have been observed previously in this region (e.g., Chavez et al. 1991) and are common among upwelling systems (reviewed Estrada and Blasco, 1985). Here we posit

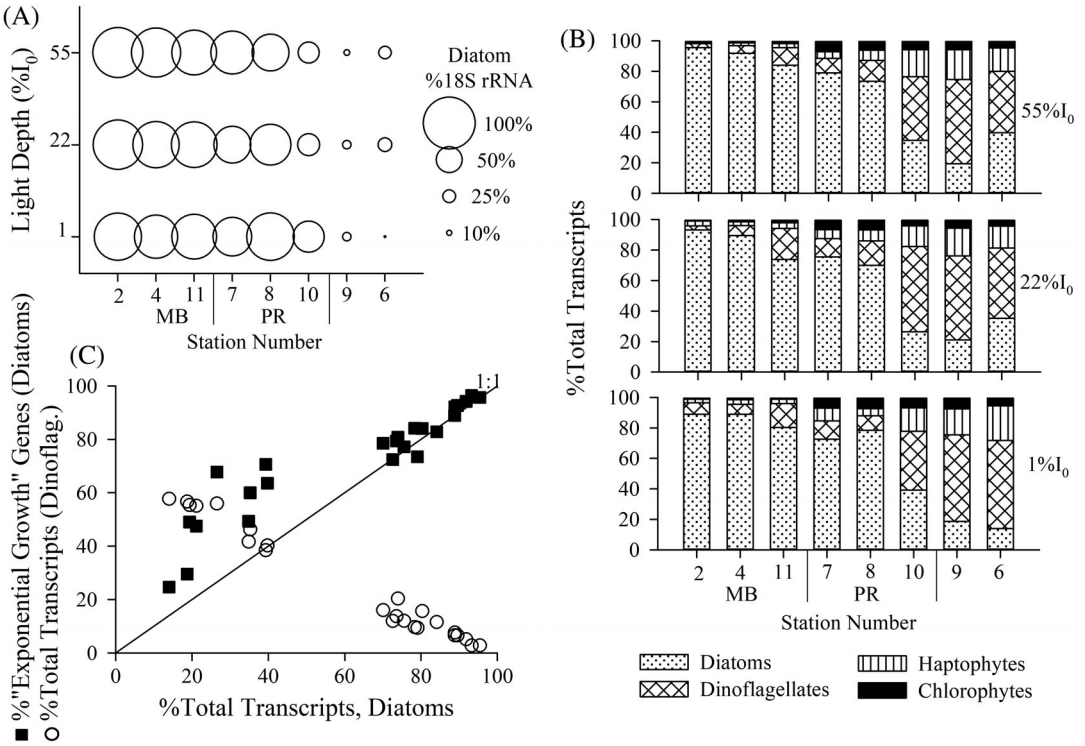


**Fig. 5.** Spatial variation in diatom composition and activity. (A) Bubble plot of diatom percentages for 18S rRNA transcription among all stations and light depths (55%, 22%, 1% $I_0$); reference bubbles offset to the right of the plot. (B) Comparison of the percent contribution of diatoms, dinoflagellates, haptophytes and chlorophytes to total transcripts among stations and light depths (55%, 22%, 1% $I_0$). (C) Comparison of the percentage of total transcripts for diatoms vs. those attributed to dinoflagellates (open circles) and the diatom contribution to "exponential growth" metric genes (Ashworth et al. 2013). Both comparisons are for all stations and depths. 1 : 1 line is shown for reference.

that mixing of coastal and offshore assemblages dilutes diatom biomass but also stimulates diatom activity, which has implications for subsequent shifts in diatom abundance with time. Without considering the physical context of rapid offshore flow, the inshore-to-offshore patterns of abundance could be interpreted erroneously as ecological succession over generations.

### Development of intense Si-uptake stress during a coastal diatom bloom

Given the strong vertical gradient in $[Si(OH)_4]$ (0.4–30 $\mu$M) over the euphotic-zone, limitation of diatom growth by $Si(OH)_4$ likely ranged from nonexistent at the highest $[Si(OH)_4]$ observed to highly probable at those stations with the lowest $[Si(OH)_4]$. Inferring growth limitation by Si using measurements of Si uptake relies on our understanding of the relationship between uptake and growth with increasing Si stress. When declining $[Si(OH)_4]$ reduces the rate of Si acquisition, diatoms first reduce their cellular silica content (Paasche 1973) to prioritize growth rate (McNair et al. 2018), maintaining rapid doubling times despite reduced uptake rates. In culture, diatoms have been observed to reduce their silica per cell up to fourfold (reviewed in Martin-Jézéquel et al. 2000). For various diatom taxa in the CCE, McNair et al. (2018) directly observed up to 2.5-fold changes in the Si content when $[Si(OH)_4]$ was depleted to ~ 2 $\mu$M, with little change to growth rate. These physiological thresholds are related to the Enh statistic. When Enh exceeds four, then the diatom assemblage may have exceeded their capacity to reduce their silica content in response to suboptimal $[Si(OH)_4]$ (Martin-Jézéquel et al. 2000); therefore, cellular Si quotas would be at their physiological minimum, and division rates would likely slow to compensate for any further reductions in uptake rate. Eq. 2 predicts Enh ~ 4 at 1.5 $\mu$M $[Si(OH)_4]$. Concentrations ≤ 1.5 $\mu$M were observed at Sta. 8 and 10 (Pt. Reyes), concurrent with near-detection-limit nutrient concentration [N + N] ~ 0.06 $\mu$M and high biomass levels [Chl *a*] ~ 2.5–10 $\mu g\ L^{-1}$ and $[bSiO_2]$ ~ 4.6–17 $\mu$mol Si $L^{-1}$. N uptake rates were not quantified during DYEatom, but on this same cruise Kranzler et al. (2019) observed that genes known to be associated with nitrate limitation were not abundant, suggesting that the diatom populations near Pt. Reyes were not N stressed. Additionally, ISIP copies among the Pt. Reyes stations were, on average, fivefold lower than in the Monterey Bay stations (Fig. 4C). These metrics suggest a peak diatom bloom condition in this domain where the biomass had become primarily limited by low Si.

The CCE regime is a "mosaic of iron limitation" (Hutchins et al. 1998; King and Barbeau 2011; Brzezinski et al. 2015). As

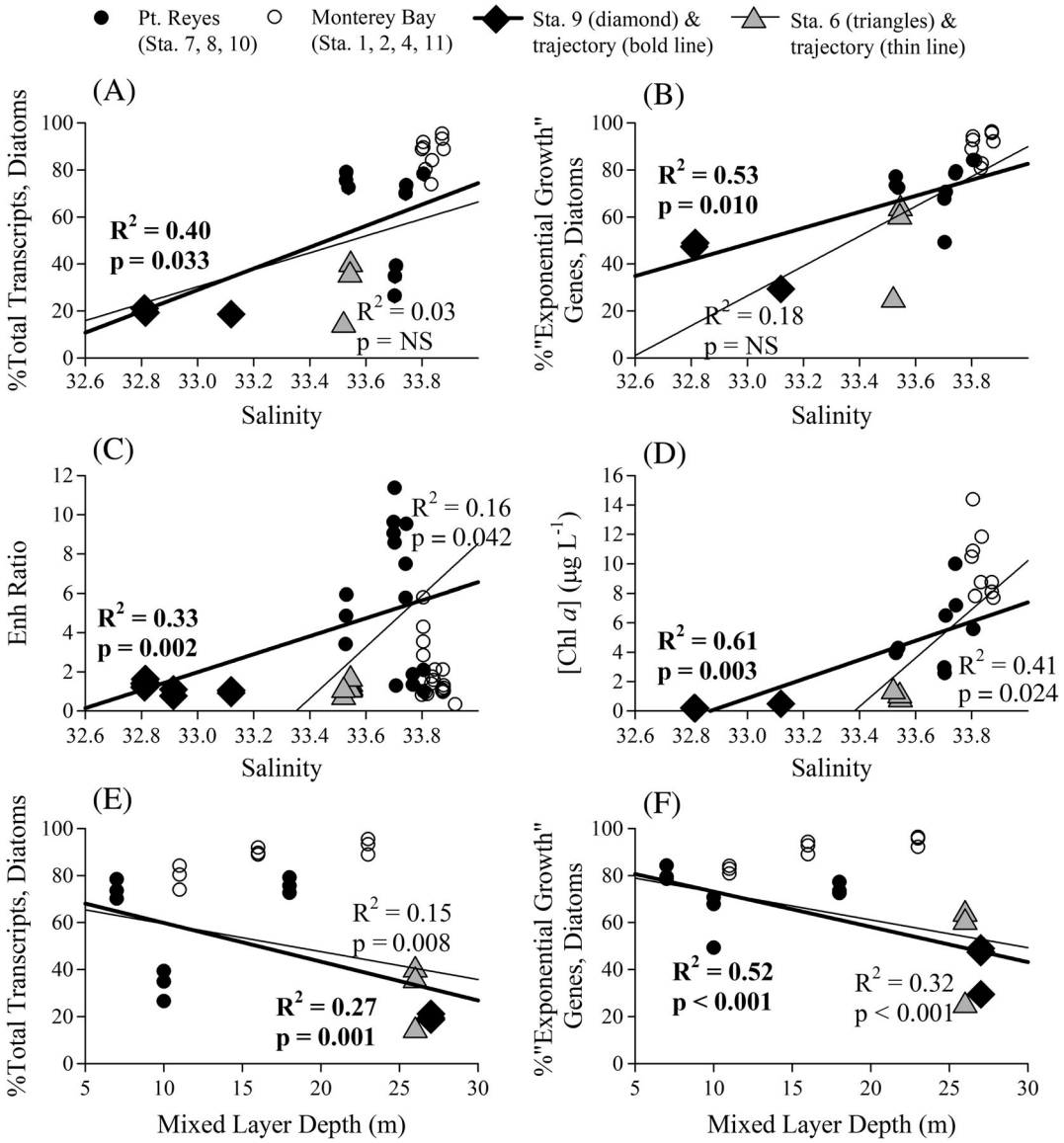


**Fig. 6.** Changes in diatom activity and phytoplankton biomass in relation to salinity (A)–(D) or mixed layer depth (E)–(F). CTD-determined salinity vs. the (A) percent diatom contribution to total phytoplankton transcripts, (B) percent diatom contribution to "exponential growth" genes, (C) Enh ratio (Fig. 4B data), and (D) chlorophyll *a* concentration. Mixed-layer depth (defined by > 0.125 kg $m^{-3}$ change from surface) vs. (E) Percent diatom contribution to total phytoplankton transcripts and (F) percent diatom contribution "exponential growth" genes. Pt. Reyes (Sta. 7, 8, and 10) and Monterey Bay (Sta. 1, 2, 4, and 11) domains denoted by filled and open circles, respectively; Sta. 6 (gray triangles) and 9 (black diamonds) are larger to emphasize trendlines. Both regressions per plot use Pt. Reyes domain inshore station (7, 8, and 10) data with either Sta. 9 (i.e., "Sta. 9 trajectory," thick line and bold font) or Sta. 6 (i.e., "Sta. 6 trajectory," thin line and regular font); Monterey Bay data are shown but not used in the regressions. Given the high precision for salinity and determining the mixed layer, Model I linear regressions were used in all panels ($R^2$ and *p*-value for the slope parameter are shown).

diatom-dominated waters were transported offshore, the effect of deepening mixed layers would likely entrain proportionally more nitrate and silicic acid than iron, due to the deepening of the ferricline offshore (King and Barbeau 2011). This may explain differences in ISIP abundance between Sta. 6 and 9. At Sta. 6 iron is presumed to be lower owing to a long transit time from inshore to offshore. Also observed is an increase in ISIP, and a shift to *Pseudo-nitzschia* spp. (Table 1; a genus well-adapted for low iron, Marchetti et al. 2009) while other nutrients (e.g., nitrate, silicic acid) may have been replenished by vertical processes. In contrast, Sta. 9 may have been less prone to iron limitation due to the position of the mesoscale feature, and the persistent offshore transport of recently-upwelled water from the Arena/Pt. Reyes upwelling cell (e.g., Bruland et al. 2001). Our transcriptomic data are thus consistent with the idea that in the absence of strong offshore advection (mesoscale eddy or jet), iron can become the limiting nutrient for diatom activity offshore and it could set the

upper limit on biomass produced in a packet of upwelled water.

While depletion of an essential limiting nutrient would be expected to result in bloom termination due to severe nutrient stress, this was not observed in our study. Despite the likely growth limitation by silicon (no sign of N limitation, Kranzler et al. 2019) and some degree of iron stress (Fig. 4C), we observed high diatom biomass (suggested by the concurrence of both high [Chl *a*] and [$bSiO_2$]) and dominance of diatom transcripts (Fig. 5B) and "exponential growth" metrics (Fig. 5C) when both [N + N] and Si were low (less than 0.1 $\mu$M and 1.5 $\mu$M, respectively). This suggests that mechanisms resupplied nutrients to surface waters, potentially due to the observed deepening of the mixed layer with offshore transport. A mechanism that could foster phytoplankton community succession, despite significant diatom growth, would be enhanced diatom mortality. There were major diatom losses due to viruses in Pt. Reyes; Kranzler et al. (2019) reported that diatom viruses were either post lytic (Sta. 7 and 8) or transitioning from active infection toward lysis (Sta. 10) on this cruise. For such loss processes to result in succession requires enough time to elapse with the water mass properties remaining relatively unchanged (e.g., low nutrients) for loss processes (e.g., grazing, viral lysis, vertical export) to remove diatoms and allow the ingrowth of dinoflagellates. The high proportion of diatom "exponential transcripts" indicated that diatom physiology was not severely compromised suggesting some process had at least partially restored diatom condition. An additional factor supporting the apparent succession observed between coastal and offshore stations is probable horizontal advection and the dilution of diatom abundance by the admixture of waters containing abundant dinoflagellates.

**Offshore advection and apparent ecological succession**

Dilution of biomass is subject to mass-balance rules, i.e., mixing two water masses equally will result in an average of their premixed biomasses. The biomass metric [Chl *a*] shows a statistically significant linear relationship with salinity, based on data from the Pt. Reyes domain and either Sta. 9 ($p = 0.003$) or Sta. 6 ($p = 0.024$) (Fig. 6D). This suggests that we resolved the mixing during offshore advection, which validates the space-for-time approach. Average [Chl *a*] and [$bSiO_2$] at Sta. 9 were lower than inshore-domain stations (7, 8, and 10) by a factor of 16 and 47, respectively, whereas biomass proxies at Sta. 6 were only 6- and 12-fold lower, respectively vs. inshore stations (7, 8, and 10). Thus, there was significant dilution and mixing of coastal water (e.g., Pt. Reyes domain origin) with offshore water.

We use these trends in biomass dilution to predict how mixing would affect diatom activity. Diatom contributions to total transcripts were lowest (14% diatom) at Sta 6 (Fig. 5B) and higher at Sta 7 (79% diatom, Fig. 5B). Given these end-member values, the 6–16-fold dilutions which are associated with mixing, should have reduced diatom contribution to "exponential growth" metrics by a similar proportion (24% at Sta. 6, 18% at Sta. 9). Instead, the diatom contribution to "exponential growth" genes at Sta. 6 and 9 was 62% and 49%, respectively, in the upper euphotic zone (> 22% $I_0$). The degree of activity enhancement, relative to that predicted by mixing, would increase if either diatoms contribution to transcripts was higher in the coastal water (e.g., 84% as in Monterey Bay) or their contribution in the low-biomass end member was lower than 14% (e.g., deep waters with low-particulate matter concentrations entrained into the euphotic zone). Thus, using conservative assumptions for diatom end-member biomass (based on total transcripts) within the space-for-time framework, this analysis suggests diatoms' contribution to "exponential growth" metrics were enhanced during offshore transport above that which is predicted by dilution (i.e., mass balance). Therefore, other factors must have been at play during transit to stimulate diatom activity.

Beyond horizontal mixing, recent analyses suggest that positive phytoplankton growth can occur when mixed layers deepen below the euphotic zone (e.g., due to nutrient entrainment—Botsford et al. 2003). Further, the Disturbance-Recovery hypothesis (Behrenfeld and Boss 2014) proposes that physical mixing and deepening of the mixed layer decouples phytoplankton growth from loss terms (e.g., zooplankton grazing, viral lysis) due to the dilution of surface waters with low-particulate deep water–reducing encounter rates. Although our data show increasing mixed-layer depth with movement offshore, the depth of the mixed layer at these stations did not exceed the depth of the euphotic zone (Table 1). The stimulatory effect in diatom "exponential growth" transcript proportion above that predicted by dilution (calculations above), may be explained by increasing access to nutrients although we have no direct data to evaluate this. The mixing (horizontal, vertical) along both trajectories (Sta. 6 and 9) clearly negated potential diatom Si limitation as observed in Sta. 8; this is demonstrated by the Enh ratios declining to values just above one at the lowest salinities (Fig. 6C), which implies no Si uptake limitation. However, consistent with the Disturbance-Recovery hypothesis, the increased vertical mixing also played a potential ecological role. During this cruise, Kranzler et al. (2019) reported that Si limitation facilitated diatom viral infection, especially in the Pt. Reyes stations; thus, in the absence of mixing, viral lysis would have been a likely end point for coastal diatoms moving offshore. We speculate that dilution of these populations during transit offshore could affect this diatom/virus dynamic in two ways: (1) stimulate diatom activity by relieving Si stress—this also would have reduced diatoms' susceptibility to viral infection (Fig. 6C), and (2) reduce the contact rates between diatoms and viruses. Advection and mixing appear to have affected either the rate of diatom growth (e.g., reduction in Si stress, increased nitrate), the ability to accumulate

biomass (e.g., reducing diatom/viral contact rates), or some combination of both.

**Conclusions**

Using an interdisciplinary approach, we suggest that physical factors prolonged the persistence of diatom-dominated upwelling communities while transporting their biomass offshore. Thus, on the scale of days, advection and increased vertical mixing in the Pt. Reyes domain appeared to play a significant role in controlling spatial distribution of phytoplankton.

While mesoscale activity appears to be a key mechanism for transporting nutrients and organic matter from the coastal environment offshore in the CCE (Nagai et al. 2015), sustaining phytoplankton biomass and organic matter production requires an active assemblage through time. Our data support previous suggestions by Halle and Largier (2011) that the eddy-like feature observed (common in this area during summer), is important for transporting high-diatom-biomass coastal waters offshore. Our analysis suggests that advection could facilitate diatom biomass accumulation through decoupling diatom growth from viral losses, potentially stimulating diatom activity by relieving nutrient limitation, or a combination of both.

## References


Alexander, H., B. D. Jenkins, T. A. Rynearson, and S. T. Dyhrman. 2015. Metatranscriptome analyses indicate resource partitioning between diatoms in the field. Proc. Natl. Acad. Sci. USA **112**: E2182–E2190.

Altschul, S. F., W. Gish, W. Miller, E. W. Myers, and D. J. Lipman. 1990. Basic local alignment search tool. J. Mol. Biol. **215**: 403–410.

Ashworth, J., S. Coesel, A. Lee, E. V. Armbrust, M. V. Orellana, and N. S. Baliga. 2013. Genome-wide diel growth state transitions in the diatom *Thalassiosira pseudonana*. Proc. Natl. Acad. Sci. USA **110**: 7518–7523.

Behrenfeld, M. J., and E. S. Boss. 2014. Resurrecting the ecological underpinnings of ocean plankton blooms. Ann. Rev. Mar. Sci. **6**: 167–194.

Botsford, L. W., C. A. Lawrence, E. P. Dever, A. Hastings, and J. Largier. 2003. Wind strength and biological productivity in upwelling systems: An idealized study. Fish. Oceanogr. **12**: 245–259.

Bruland, K. W., E. L. Rue, and G. J. Smith. 2001. Iron and macronutrients in California coastal upwelling regimes: Implications for diatom blooms. Limnol. Oceanogr. **46**: 1661–1674.

Brzezinski, M. A., and D. R. Phillips. 1997. Evaluation of Si-32 as a tracer for measuring silica production rates in marine waters. Limnol. Oceanogr. **42**: 856–865.

Brzezinski, M. A., D. R. Phillips, F. P. Chavez, G. E. Friederich, and R. C. Dugdale. 1997. Silica production in the Monterey, California, upwelling system. Limnol. Oceanogr. **42**: 1694–1705.

Brzezinski, M. A., and L. Washburn. 2011. Phytoplankton primary productivity in the Santa Barbara Channel: Effects of wind-driven upwelling and mesoscale eddies. J. Geophys. Res. **116**: C12013.

Brzezinski, M. A., J. L. Jones, K. D. Bidle, and F. Azam. 2003. The balance between silica production and silica dissolution in the sea: Insights from Monterey Bay, California, applied to the global data set. Limnol. Oceanogr. **48**: 1846–1854.

Brzezinski, M. A., and others. 2015. Variable influence of iron stress on siliceous biomass and silica production and silicon and carbon export in a frontal zone within the California Current. J. Geophys. Res. Oceans **120**: 4654–4669.

Caron, D. A., and others. 2017. Probing the evolution, ecology and physiology of marine protists using transcriptomics. Nat. Rev. Microbiol. **15**: 6–20.

Carradec, Q., and others. 2018. A global ocean atlas of eukaryotic genes. Nat. Commun. **9**: 373.

Chavez, F. P., and others. 1991. Horizontal transport and the distribution of nutrients in the coastal transition zone off northern California: Effects on primary production, phytoplankton biomass and species composition. J. Geophys. Res. Oceans **96**: 14833–14848.

Cianelli, D., and others. 2017. Disentangling physical and biological drivers of phytoplankton dynamics in a coastal system. Sci. Rep. **7**: 15868.

d'Ovidio, F., S. De Monte, S. Alvain, Y. Dandonneau, and M. Lévy. 2010. Fluid dynamical niches of phytoplankton types. Proc. Natl. Acad. Sci. USA **107**: 18366–18370.

De Vargas, C., and others. 2015. Eukaryotic plankton diversity in the sunlit ocean. Science **348**: 1261605.

Edgar, R. C. 2010. Search and clustering orders of magnitude faster than BLAST. Bioinformatics **26**: 2460–2461.

Estrada, M., and D. Blasco. 1985. Phytoplankton assemblages in coastal upwelling areas. Int. Symp. Upwelling W. Africa, Inst. Invest. Pesq. Barcelona 1: 379–402.

Gaube, P., D. B. Chelton, P. G. Strutton, and M. J. Behrenfeld. 2013. Satellite observations of chlorophyll, phytoplankton biomass, and Ekman pumping in nonlinear mesoscale eddies. J. Geophys. Res. Oceans **118**: 6349–6370.

Halle, C. M., and J. L. Largier. 2011. Surface circulation downstream of the point arena upwelling center. Cont. Shelf Res. **31**: 1260–1272.

Hutchins, D., G. DiTullio, Y. Zhang, and K. Bruland. 1998. An iron limitation mosaic in the California upwelling regime. Limnol. Oceanogr. **43**: 1037–1054.

Kaplan, D. M., and J. Largier. 2006. HF radar-derived origin and destination of surface waters off Bodega Bay, California. Deep-Sea Res. II **53**: 2906–2930.

King, A. L., and K. A. Barbeau. 2011. Dissolved iron and macronutrient distributions in the southern California Current System. J. Geophys. Res. Oceans **116**: C03018..

Kranzler, C. F., and others. 2019. Silicon limitation facilitates virus infection and mortality of marine diatoms. Nat. Microbiol. **4**: 1790–1797.

Krause, J. W., M. A. Brzezinski, and J. L. Jones. 2011. Application of low level beta counting of $^{32}$Si for the measurement of silica production rates in aquatic environments. Mar. Chem. **127**: 40–47.

Krause, J. W., M. A. Brzezinski, T. A. Villareal, and C. Wilson. 2012. Increased kinetic efficiency for silicic acid uptake as a driver of summer diatom blooms in the North Pacific Subtropical Gyre. Limnol. Oceanogr. **57**: 1084–1098.

Krause, J. W., and others. 2015. Variability in diatom contributions to biomass, organic matter production, and export across a frontal gradient in the California current ecosystem. J. Geophys. Res. Oceans **120**: 1032–1047.

Lampe, R. H., and others. 2018. Divergent gene expression among phytoplankton taxa in response to upwelling. Environ. Microbiol. **20**: 3069–3082.

Largier, J., B. Magnell, and C. Winant. 1993. Subtidal circulation over the northern California shelf. J. Geophys. Res. Oceans **98**: 18147–18179.

Largier, J. L., and others. 2006. WEST: A northern California study of the role of wind-driven transport in the productivity of coastal plankton communities. Deep-Sea Res. II **53**: 2833–2849.

Lassiter, A. M., F. P. Wilkerson, R. C. Dugdale, and V. E. Hogue. 2006. Phytoplankton assemblages in the CoOP-WEST coastal upwelling area. Deep-Sea Res. II **53**: 3063–3077.

Lomas, M. W., F. Lipschultz, D. M. Nelson, J. W. Krause, and N. R. Bates. 2009. Biogeochemical responses to late-winter storms in the Sargasso Sea, I—Pulses of primary and new production. Deep-Sea Res. I **56**: 843–860.

Lomas, M. W., J. A. Bonachela, S. A. Levin, and A. C. Martiny. 2014. Impact of ocean phytoplankton diversity on phosphate uptake. Proc. Natl. Acad. Sci. USA **111**: 17540–17545.

Mahé, F., T. Rognes, C. Quince, C. de Vargas, and M. Dunthorn. 2015. Swarm v2: Highly-scalable and high-resolution amplicon clustering. PeerJ **3**: e1420.

Marchetti, A., and others. 2009. Ferritin is used for iron storage in bloom-forming marine pennate diatoms. Nature **457**: 467–470.

Margalef, R. 1978. Life-forms of phytoplankton as survival alternatives in an unstable environment. Oceanol. Acta **1**: 493–509.

Martin-Jézéquel, V., M. Hildebrand, and M. A. Brzezinski. 2000. Silicon metabolism in diatoms: Implications for growth. J. Phycol. **36**: 821–840.

McNair, H. M., M. A. Brzezinski, and J. W. Krause. 2018. Diatom populations in an upwelling environment decrease silica content to avoid growth limitation. Environ. Microbiol. **20**: 4184–4193.

Nagai, T., N. Gruber, H. Frenzel, Z. Lachkar, J. C. McWilliams, and G. K. Plattner. 2015. Dominant role of eddies and filaments in the offshore transport of carbon and nutrients in the California current system. J. Geophys. Res. Oceans **120**: 5318–5341.

Nelson, D. M., M. A. Brzezinski, D. E. Sigmon, and V. M. Franck. 2001. A seasonal progression of Si limitation in the Pacific sector of the Southern Ocean. Deep-Sea Res. II **48**: 3973–3995.

Paasche, E. 1973. Silicon and the ecology of marine plankton diatoms. I. Thalassiosira pseudonana (*Cyclotella nana*) grown in a chemostat with silicate as limiting nutrient. Mar. Biol. **19**: 117–126.

Pearson, W. R. 2016. Finding protein and nucleotide similarities with FASTA. Curr. Protoc. Bioinformatics **53**: 3.9.1-25.

Pickett, S. T. 1989. Space-for-time substitution as an alternative to long-term studies, p. 110–135. *In* Long-term studies in ecology. Springer.

Reynolds, C. S. 1984. The ecology of freshwater phytoplankton. Cambridge Univ. Press.

Rho, M., H. Tang, and Y. Ye. 2010. FragGeneScan: Predicting genes in short and error-prone reads. Nucleic Acids Res. **38**: e191–e191.

Schmieder, R., Y. W. Lim, and R. Edwards. 2011. Identification and removal of ribosomal RNA sequences from metatranscriptomes. Bioinformatics **28**: 433–435.

Sonnhammer, E. L., S. R. Eddy, E. Birney, A. Bateman, and R. Durbin. 1998. Pfam: Multiple sequence alignments and HMM-profiles of protein domains. Nucleic Acids Res. **26**: 320–322.

Stoeck, T., D. Bass, M. Nebel, R. C. Jones, M. D. M. Jones, H. W. Breiner, T.A. Richards. 2010. Multiple marker parallel tag environmental DNA sequencing reveals a highly complex eukaryotic community in marine anoxic water. Molecular Ecology **19**:21–31.

Stukel, M. R., and others. 2017. Mesoscale Ocean fronts enhance carbon export due to gravitational sinking and subduction. Proc. Natl. Acad. Sci. USA **114**: 1252–1257.

Taylor, A. G., R. Goericke, M. R. Landry, K. E. Selph, D. A. Wick, and M. J. Roadman. 2012. Sharp gradients in phytoplankton community structure across a frontal zone in the California Current Ecosystem. J. Plankton Res. **34**: 778–789.

Teng, Y.-C., F. W. Primeau, J. K. Moore, M. W. Lomas, and A. C. Martiny. 2014. Global-scale variations of the ratios of carbon to phosphorus in exported marine organic matter. Nat. Geosci. **7**: 895.

Tilman, D. 1977. Resource competition between planktonic algae: An experimental and theoretical approach. Ecology **58**: 338–348.

Tilman, D., S. S. Kilham, and P. Kilham. 1982. Phytoplankton community ecology: The role of limiting nutrients. Annu. Rev. Ecol. Syst. **13**: 349–372.

Villar, E., and others. 2015. Environmental characteristics of Agulhas rings affect interocean plankton transport. Science **348**: 1261447.

Wilkerson, F. P., A. M. Lassiter, R. C. Dugdale, A. Marchi, and V. E. Hogue. 2006. The phytoplankton bloom response to

wind events and upwelled nutrients during the CoOP WEST study. Deep-Sea Res. II **53**: 3023–3048.

Zhang, Y., and others. 2019. Metatranscriptomic signatures associated with phytoplankton regime shift from diatom dominance to a dinoflagellate bloom. Front. Microbiol. **10**: 590.

## Acknowledgments

We thank the following for shipboard support: J. L. Jones, E. Lachenmyer, I. Marquez, M. Johnson, B. Edwards, J. Ossolinski, Captain R. Verlini, Marine Technician S. Alesandrini and crew of the R/V Pt. Sur, and D. Shideler and M. Losekoot for support in obtaining high-frequency radar data as part of the Central and Northern California Ocean Observing System. This work was supported by grants from the National Science Foundation (OCE-1155663 to JWK; OCE-1333929 to KT; OCE-1334387 to MAB; OCE-1756884 to AEA), the Gordon and Betty Moore Foundation (GBMF3789 to KDB), and NOAA (NA15OAR4320071 to AEA; CeNCOOS to JLL). Metatranscriptomic data is available in the NCBI sequence read archive (BioProject accession no. PRJNA528986: BioSample accession nos. SAMN11263616–SAMN11263639 and SAMN11258802–SAMN11258825). Assembled contigs can be found at https://scripps.ucsd.edu/labs/aallen/data/ and BCO-DMO project number 558198 (www.bco-dmo.org/project/558198). All other cruise-related data are available publicly at www.bco-dmo.org/project/550825.

## Conflict of Interest

None declared.

*Submitted 23 August 2019*
*Revised 20 December 2019*
*Accepted 03 February 2020*

*Associate editor: Birte Matthiessen*